MOEM

Modern Electronic Materials 2024; 10(4): 207–216
DOI 10.3897/j.moem.10.4.136067

Research Article

Additive contribution of multiferroic film and semiconductor substrate from nanotube array to resistive switching, topographic features

Shikhgasan Ramazanov[1], Gaji Gajiev[1], Daud Selimov[1], Sadrudin Gadzhimuradov[1], Sagim Suleymanov[1], Ştefan Ţălu[2], Robert S. Matos[3], Henrique D. da Fonseca Filho[4]

1 *Amirkhanov Institute of Physics, Dagestan Federal Research Center of the Russian Academy of Sciences, 94 Magomed Yaragsky Str., Makhachkala, Republic of Dagestan 367003, Russian Federation*

2 *Technical University of Cluj-Napoca, Directorate of Research, Development and Innovation Management, 15 Constantin Daicoviciu Str., Cluj-Napoca 400020, Romania*

3 *Universidade Federal do Amapá, Amazonian Materials Group, Departamento de Física, 68903-419, Macapá, Amapá, Brazil*

4 *Universidade Federal do Amazonas, Laboratory of Synthesis of Nanomaterials and Nanoscopy, Departamento de Física, 69067-005, Manaus, Amazonas, Brazil*

Corresponding author: Shikhgasan Ramazanov (ramazanv@mail.ru)

Received 1 September 2024 ♦ **Accepted** 21 November 2024 ♦ **Published** 30 December 2024

Citation: Ramazanov Sh, Gajiev G, Selimov D, Gadzhimuradov S, Suleymanov S, Ţălu Ş, Matos RS, da Fonseca Filho HD (2024) Additive contribution of multiferroic film and semiconductor substrate from nanotube array to resistive switching, topographic features. *Modern Electronic Materials* 10(4): 207–216. https://doi.org/10.3897/j.moem.10.4.136067

Abstract

The structure $BiFeO_3/TiO_2$–NTs (BFOT) obtained using the atomic layer deposition. During the Anatase/Rutile phase transformation; there is a redistribution of Fe/Ti atoms, resulting in the formation of local inhomogeneities and charge trapping centres. Studies of the resistive switching effect showed nonlinear current-voltage characteristics. The negative differential resistance probably arises from the oxide dielectric layer of BFO, thin regions of which participate in the tunneling process. The BFOT surface exhibits topographic variations with spatial patterns that conform to normality, and the distribution of topographic heights displays a quasi-normal behavior. The self-affine attributes of the BFOT film are validated by the exponential reduction in autocorrelation functions, and the Minkowski functionals underscore the intricate and irregular nature of the film's topographic patterns.

Keywords

atomic layer deposition, $BiFeO_3$, resistive switching, TiO_2 nanotubes, Minkowski functionals, negative differential resistance

1. Introduction

The interest in various phenomena of electrical conductivity changes, such as negative differential resistance, threshold switching, and memory switching observed in a range of insulating and semiconductor materials, is steadily increasing [1, 2]. With the development of new methods for determining characteristics and sample preparation technologies, as well as the discovery of ferroelectric and antiferromagnetic behavior in $BiFeO_3$ (BFO) films in recent decades, interest in the application of thin multifunctional ferroelectric films for next-gen-

eration devices has grown. The properties of BFO vary depending on the size of the nanoparticles [3, 4].

Layered ferroelectrics, often called natural superlattices, have functional capabilities that exceed those of classical perovskite ferroelectric compounds due to their highly anisotropic structure. The family of bismuth compounds with the Aurivillius layered structure has attracted a lot of attention due to the remarkable characteristics of the multiferroic: absence of lead/fatigue and high Curie temperature (T_C). In the ultra-thin regime, layered structure films demonstrate flat polarization with periodic arrangement of ferroelectric domains, which, with uniaxial ferroelectric anisotropy, leads to nominally charged domain walls. The layered phase is an infinitely adaptive structure in which each composition is ordered into a superlattice. These properties make it a potential application as energy-independent random access memory devices.

In the early 1970s, Chua proposed a theoretical model describing the relationship between the voltage applied to an element and the time integral of current [5]. He described the operation of a fourth fundamental circuit element, which he named the "memristor". A memristor can be described as a two-terminal device with a nonlinear current-voltage characteristic and exhibiting a certain degree of hysteresis. Similar to a synapse, the resistance of a memristor changes based on the pulses applied to the "presynaptic" and "postsynaptic" terminals, thereby implementing rules of plasticity that depend on the timing and frequency of the pulses. The switching effect (RS) in ferroelectric materials can be induced by modulating interfacial barriers through polarization switching, migration of ionic defects, trapping/releasing of charge carriers, as well as the formation and rupture of conductive filaments [6–9]. Memristors are one of the most promising elements of modern microelectronics, possessing unique properties such as quasi-continuous conductivity changes and long-lasting resistive states [10, 11]. The artificially modulated structure in the Aurivillius phase forms a one-dimensional periodic potential that significantly affects the energy spectrum of electrons. Such a quasi-stable state throughout the volume will allow operation at low voltages, which is important for reducing the contribution of thermal effects in nanoelectronic devices. In this work, the object of study was a heterostructure based on BFOT.

2. Materials and methods

BFO films were grown by atomic layer deposition (ALD) using ALDCERAM ML-200. A titanium plate was used as a substrate, on which a TiO_2–NTs was previously obtained by electrochemical deposition in the form of vertical array of nanotubes. The thickness of the TiO_2–NTs layer was ~2.5 μm. Bi(*mmp*)$_3$ and ferrocene Fe(*cp*)$_2$ were used as precursor sources [12, 13]. For electrical measurements, contacts were applied to the surface using magnetron sputtering. To understand the thermodynamics of the formation of Bi–O and Fe–O layers, quantum-chemical calculations were conducted to study the layer-by-layer progression of the reaction with ozone. The thickness of the obtained BFO film is ~80 nm.

Figure 1 presents the experimentally obtained values for determining the temperature window of mass increase using each precursor individually, as well as the dependence of $\Delta G(T)$.

The quantum-chemical calculations show good agreement with the experimental data. As seen from the mass increase graph, the bismuth precursor begins to decompose in the gas phase as the temperature rises, while the iron precursor continues to grow. An increase in temperature may further promote the reaction of the resulting products with oxygen. It has been noted that the most favorable low-temperature reaction for the formation of iron oxide occurs with ozone [14].

Electrical measurements were performed using a Rigol MSO4034 digital oscilloscope and an Agilent 81150A-001 signal generator. The voltage sweep for the $I(V)$ measurement was in the form of a bidirectional triangular waveform.

SEM images were made by high resolution scanning electron microscope VERIOS 460L (Thermo Fisher Scientific, Waltham, USA). The electron beam current was 25 pA and voltage was 3 kV. Secondary electrons were collected by through-the-lens detector. The working distance was 3.5 mm. The SEM images (1600×1200 pixels) were captured at ×200 to 140 000 magnification. The AFM topographies of the composite layers were recorded in atmospheric conditions (at a temperature of 23 °C and less than 60% relative humidity) in non-contact mode on a surface area of 5×5 μm^2. The AFM studies were done using a NT-MDT NTEGRA Probe Nano Laboratory instrument (NT-MDT, Moscow, Russia).

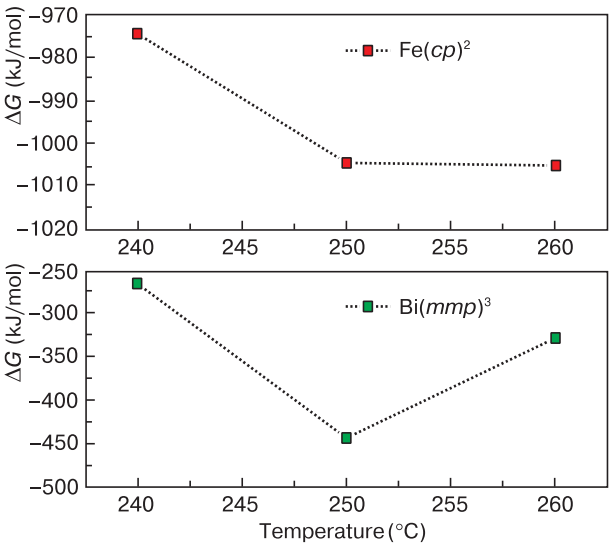

Figure 1. The temperature dependence of the Gibbs free energy when using iron and a bismuth-containing precursor in the reaction with ozone (the line is a guide for the eyes)

The AFM instrument was equipped with a silicon NT-MDT NSG01 cantilever (NT-MDT, Moscow, Russia) with the following features: length 125 μm, width 30 μm, thickness 1.5–2.5 μm, tip curvature radius 10 nm; resonant frequency 87–230 kHz, and force constant 1.45–15.1 N/m. Five images were recorded on different reference areas of the sample to obtain a representative average of the analysis parameter. The morphological analysis and correlated parameters of the sample were evaluated using the Gwyddion 2.59 software for precise topographical characterization [15].

The statistical analysis was performed using the GraphPadInStat version 5.0 software package, developed by GraphPad in San Diego, California, USA. The statistical analysis began with checking the normality of data using the Shapiro–Wilk test, then proceeded to use parametric (T-test) and non-parametric (Mann-Whitney U-test) tests, with a threshold for significance set at $p < 0.05$. Finally, the results were presented in terms of mean and standard deviation, which provided an overview of the central tendency and variability of the data.

To study the nonlinear properties of the memristor, the SPICE model (Simulation Program with Integrated Circuit Emphasis) was used [16]. This paper discusses a nonlinear drift memristor model that incorporates a modified Biolek window function and an activation threshold, improving simulation accuracy for applications in electronics. The model addresses issues of nonlinearity and window functions in memristor behavior, providing more realistic and adaptable simulations for our system.

3. Results and discussion

In the Bi–O layer of the TiO_2–Bi_2O_3–TiO_2 "sandwich" composition, a stable compound B $Bi_4Ti_3O_{12}$ is formed by diffusion of titanium, as reported in [17]. The anneal-

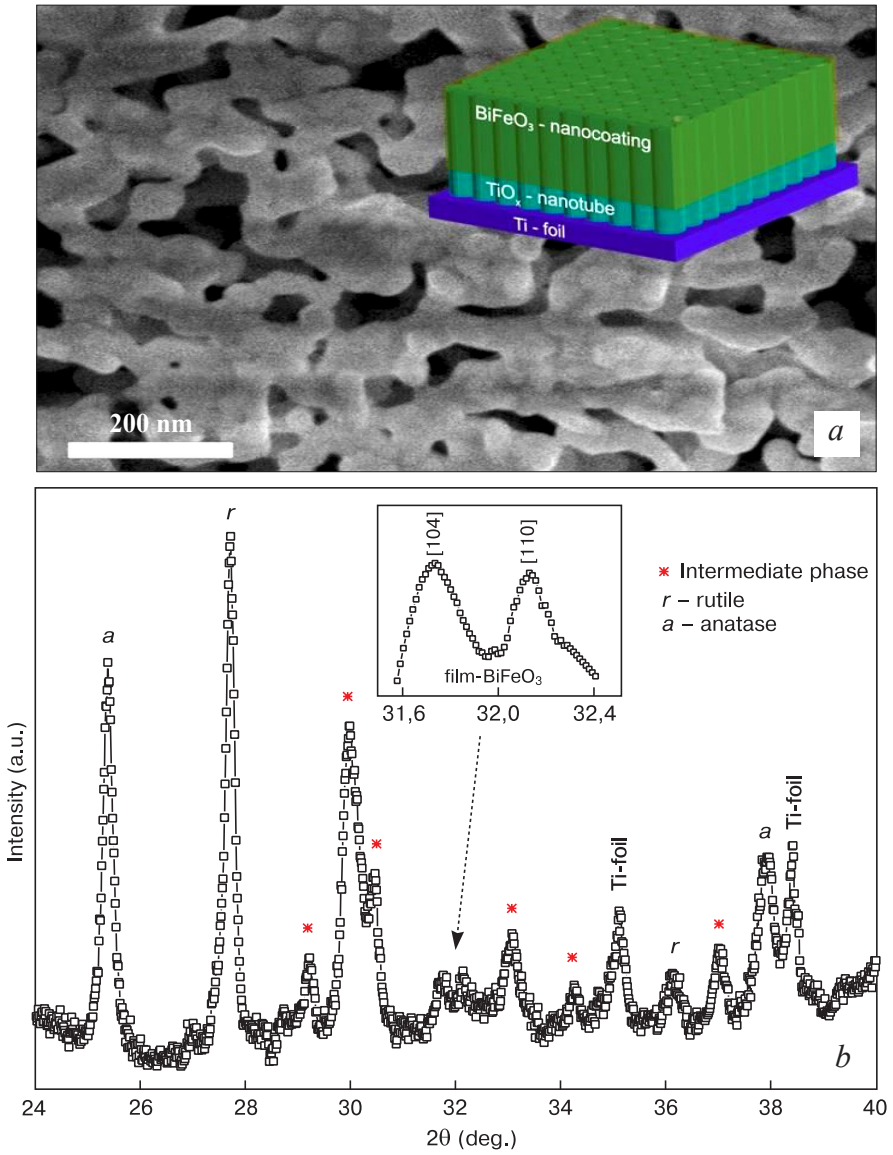

Figure 2. (*a*) SEM image of the BFOT sample surface, on the tab the structure of the obtained two-layer composite, (*b*) X-ray diffraction analysis of BFOT sample

ing temperature of 660 °C is close to the melting temperature of the γ-Bi_2O_3 phase ($T_m \approx 550$–630 °C), at which the mass transfer rate sharply increases and chemical reactions are initiated. In the Bi_2O_3/FeO_x region, the reaction proceeds via mass transfer to form the BFO phase [18]. Sequential reactions during thermal treatment promote self-organization of the Aurivillius phases of the $BiFeO_3$–$Bi_4Ti_3O_{12}$ system [19]. Figure 2 shows an SEM image of the surface of the obtained film and X-ray diffraction analysis.

As can be seen from the XRD (Fig. 2*b*), the sample consists of anatase and rutile TiO_2 phases, a BFO film, and intermediate phases (bismuth titanate and Aurivilius phase). Experimental data on the kinetics of layered perovskite-like compounds formation in the BFTO system showed that the Aurivillius phase begins to form already at 600 °C. The crystal lattice of all Aurivillius phases is built of perovskite-like layers $(A_{n-1}B_nO_{3n+1})^{2-}$ (these are peaks in the 30° region Fig. 2*b*), which alternate with bismuth-oxygen layers $(Bi_2O_2)^{2+}$. Phase-modulated structures may arise at the interface of BFOT with nanotubes. Modulation of the interface in periodically arranged structures has been reported earlier, but it was usually achieved by doping different positions in the structure with alkaline earth or rare earth metal ions [17]. The transition between layers with different numbers of blocks is accompanied by defects in the $(Bi_2O_2)^{2+}$ layer arrangement. However, the perovskite structure is maintained, and regular lattice distortions are formed in specific areas, forming regions with morphotropic phase transitions. These regions are likely associated with the substitution of Fe^{3+} ions in a narrow range of 0.58–0.65 by Ti^{4+} ions in octahedral cells. The ion displacements relative to the $(Bi_2O_2)^{2+}$ layer are related to the difference in iron and titanium ionic radii of ~6%.

The ALD process enables complete coverage of all regions of the nanotubes, effectively infiltrating their depths and partially sealing the pores within. The resulting rough peaks form 3D spatial patterns with significant heterogeneity, resulting in a surface characterized by high roughness. Figure 3 depict AFM images in both 2D and 3D formats of the sample, and the distribution of crystallite

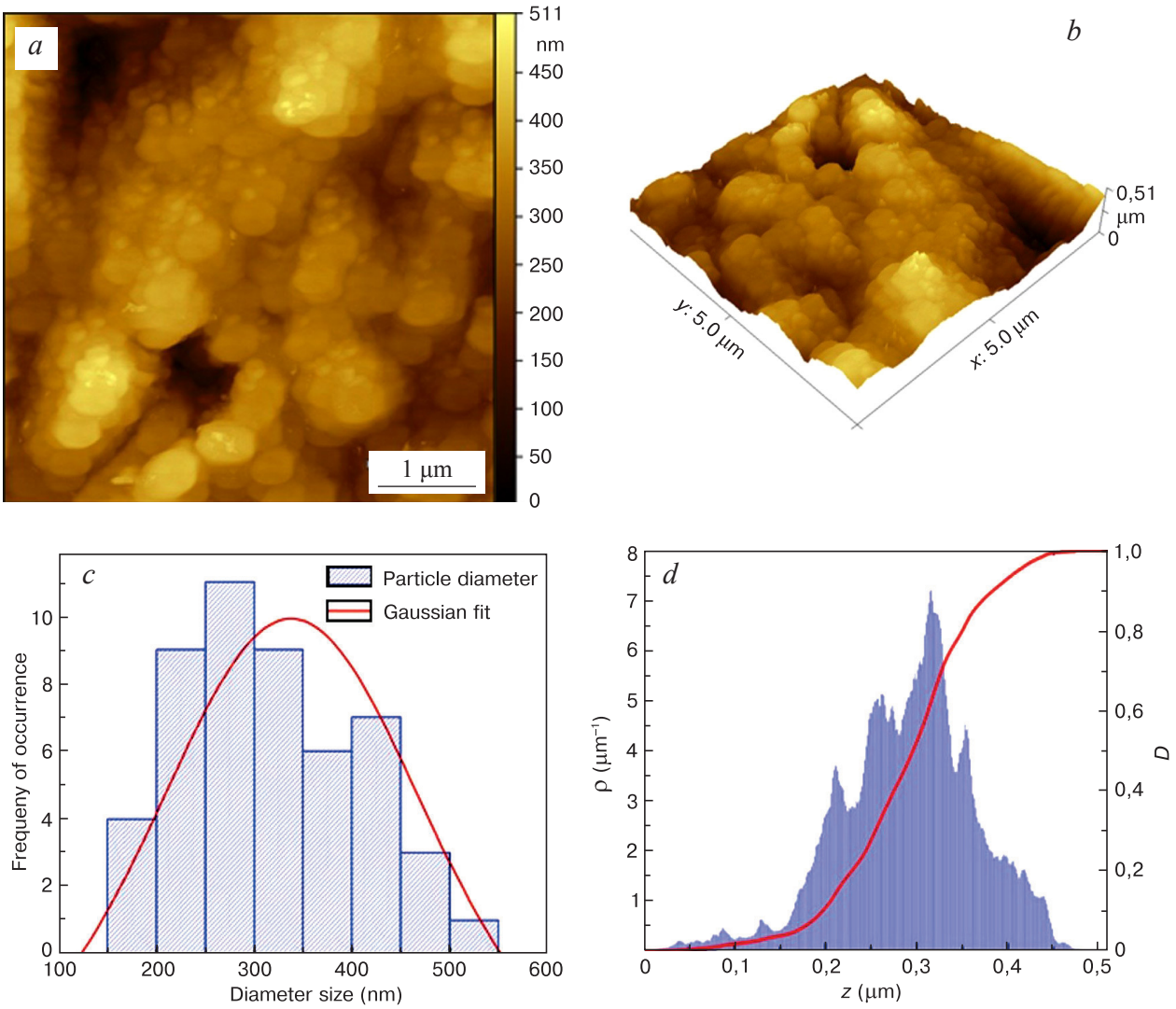

Figure 3. (*a*) 2D AFM image, (*b*) 3D AFM image, (*c*) height distribution, (*d*) Abbot Firestone curve of the BFOT representative sample surface

Table 1. Height statistical surface parameters of the BFOT sample

Sample	S_q (nm)	S_a (nm)	S_{sk}	S_{ku}	S_p (nm)	S_v (nm)	S_z (nm)
BFOT	74.73	58.63	–0.42	3.4758	220.66	290.69	511.35

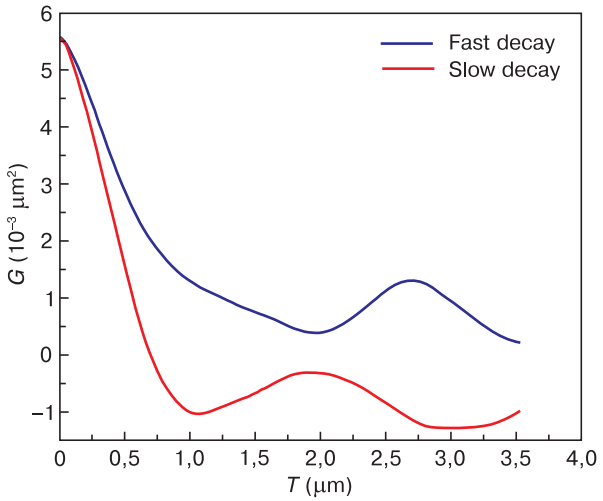

Figure 4. The autocorrelation functions (ACFs) as a function of the sample length (r) of BFOT sample

grains on the surface is shown, Abbot Firestone curve of the sample.

The particle size distribution for the BFOT coatings, as shown in Fig. 3*c*, highlights a near-normal distribution pattern, with particle diameters predominantly ranging between 160 and 500 nm. The Gaussian fit (red line) in the figure demonstrates that the frequency of occurrence of particle sizes is highest within this interval, indicating a relatively uniform particle size across the sample. This distribution suggests that the ALD process effectively produces particles of a consistent size, which is crucial for achieving homogeneous film properties. The Gaussian behavior of the particle size distribution also underscores the controlled conditions during the ALD process, essential for optimizing the coating's functional attributes. The large sizes of crystallites are also associated with the sizes of the original nanotubes themselves, with diameters of about ~130 nm [19]. The distribution of topographic heights displays a quasi-normal behavior, with the bulk of topographic heights concentrated between 200 and 400 nm (Fig. 3*d*). The high asperity is attributed to the pronounced non-uniformity of the nanotube array, giving rise to elevated roughness values. The red S-shaped line in Fig. 3*d* represents the behavior of the Abbot Firestone curve for the 3D surface topographical profile. A typical pattern of rough surfaces is observed thanks to the well-defined shape of the Abbot Firestone curve. This confirms that the density of the topographic height distribution rapidly reaches its maximum following the S-shaped regime, affirming the nearly normal behavior of the topographic height distribution. This suggests that the BFOT surface exhibits topographic variations but is comprised of spatial patterns that conform to normality, ultimately yielding a uniform surface.

The surface of the BFOT film displays an average roughness (S_a) and root mean square roughness (S_q) of 58.63 and 74.73 nm (Table 1), respectively. These values are notably elevated compared to the 6.35 nm reported by Xie et al. [20] for a BFO film. This discrepancy underscores the significant influence of nanotubes in shaping the rough surface of BFOT. The elevated surface roughness is further substantiated by other height-based surface statistical parameters, including maximum peak height (S_p), maximum valley depth (S_v), and maximum valley depth (S_z), as outlined in Table 1. The nearly normal behavior of the height distribution is validated by the surface kurtosis value ($S_{ku} \sim 3$), indicating that the BFOT film surface displays an quasi platykurtic pattern [21, 22]. Moreover, even though the distribution of topographic heights is right-skewed ($S_{sk} < 0$), its value approaches zero, signifying an almost perfect symmetry in height distribution. Both S_{ku} and S_{sk} affirm that the distribution of topographic heights approximates a nearly normal distribution, underscoring the tendency of spatial patterns to exhibit uniformity [23].

The autocorrelation functions (ACFs) representative of the 3D spatial patterns of BFOT film are depicted in Fig. 4.

We leverage these ACFs to evaluate the surface's isotropic characteristics, benefitting from their correlation with microtexture and topographical roughness [24]. Notably, the ACF curves disclose both the slowest and fastest decay rates, obtained using normalized ACFs, with their respective parameters outlined in Table 2. The self-affine attributes of the BFOT film are validated by the exponential reduction in ACFs [25], transitioning from a value of $6 \cdot 10^{-3}$ to 0 along different directions for the fastest (τ_{a1}) and slowest (τ_{a2}), as detailed in Table 2.

Table 2. The fastest (τ_{a1}) and the slowest (τ_{a2}) decay directions, decay lengths (S_{a1} and S_{a2}), and anisotropy factor (S_{tr}) for the investigated sample

Sample	τ_{a1} (deg)	τ_{a2} (deg)	S_{a1} (nm)	S_{a2} (nm)	S_{tr}
BFOT	–27.26	66.80	90.63	130.2	0.6963

It's worth noting that the fastest autocorrelation decay (S_{a1}) and slowest autocorrelation decay (S_{a2}) are notably high, affirming the coarse features of the BFOT surface, a hallmark of isotropic surfaces, as visually evident in Fig. 2. This behavior is likely attributed to the rounded structures constituting the surface microtexture of the film. Furthermore, the texture aspect ratio (S_{tr}) is determined to exceed 0.5, unequivocally confirming the pronounced isotropic nature of the film. This isotropy arises from the distinctive organization of its 3D spatial patterns.

Consequently, the distribution of topographical heights across the film engenders spatial patterns that are nearly symmetrical and platykurtic, imparting a high degree of surface isotropy to the film. These characteristics can have notable effects on various physical properties, e.g., wettability, adhesion, and wear resistance [21].

The film's surface characteristics underwent further examination using Minkowski functionals (MFs), as illustrated in Fig. 5. MFs essential in surface analysis, offer a structured approach to quantify surface attributes such as volume, boundary, and connectivity [26], which are calculated as follow.

In Gwyddion 2.59 software [15] (V is calculated as the cumulative volume above or below a reference plane. This volume is measured by integrating the height values over the surface area:

$$V = \sum_{i,j} h_{ij} \times A_{\text{pixel}}, \quad (1)$$

where h_{ij} is the height of the surface at each pixel i, j, and A_{pixel} is the area of each pixel. This approach sums the height values above the reference plane, giving a volumetric measure of the topography.

The surface area S in Gwyddion is the total area of the 3D surface, taking into account the slope between neighbouring pixels. Instead of simply summing flat pixel areas, Gwyddion uses a triangulated approach to account for surface curvature:

$$S = \sum_{i,j} \sqrt{1 + \left(\frac{\partial h}{\partial x}\right)^2 + \left(\frac{\partial h}{\partial y}\right)^2} \times A_{\text{pixel}}, \quad (2)$$

where $\partial h/\partial x$ and $\partial h/\partial y$ represent the partial derivatives of the height field with respect to x and y, respectively, which Gwyddion estimates from adjacent pixels to approximate local slopes. This formula accounts for the "true" 3D area of the surface, not just the projected area.

The Euler characteristic χ, or connectivity, is calculated in Gwyddion by counting features based on connected regions of pixels above or below a certain threshold. This value essentially represents the number of connected components minus the number of holes:

$$\chi = N_{\text{components}} - N_{\text{holes}}, \quad (3)$$

where Gwyddion identifies each connected component (such as peaks or voids) and counts them, adjusting for holes or "islands" that may exist within these components. The software does this by thresholding the height values and examining connected clusters of pixels to determine $N_{\text{components}}$ and N_{holes}.

In Fig. 4*a*, we note a consistent decrease in Minkowski volume concerning relative height (in μm) across all biofilms. This signifies a substantial presence of matter above the specified height, reflecting the film's coarse nature. Figure 5*b* reveals the Minkowski boundary (S) exhibiting non-monotonic behavior with respect to relative height (%). This observation is supported by the holes over the surface that are concentrated within the topographic height range of 0.2 to 0.4 μm, coinciding with the distinctive height topographical profile seen in Fig. 3*c*. Notably, this is linked to the film's surface displaying topographic variations across multiple scales due to its high roughness. Finally, Fig. 5*c* reveals the Minkowski connectivity (χ) that was projected without prominent minima or maxima. Instead, it showcases a random distribution of connectivity values, primarily due to the film's inherent surface heterogeneity. This observation

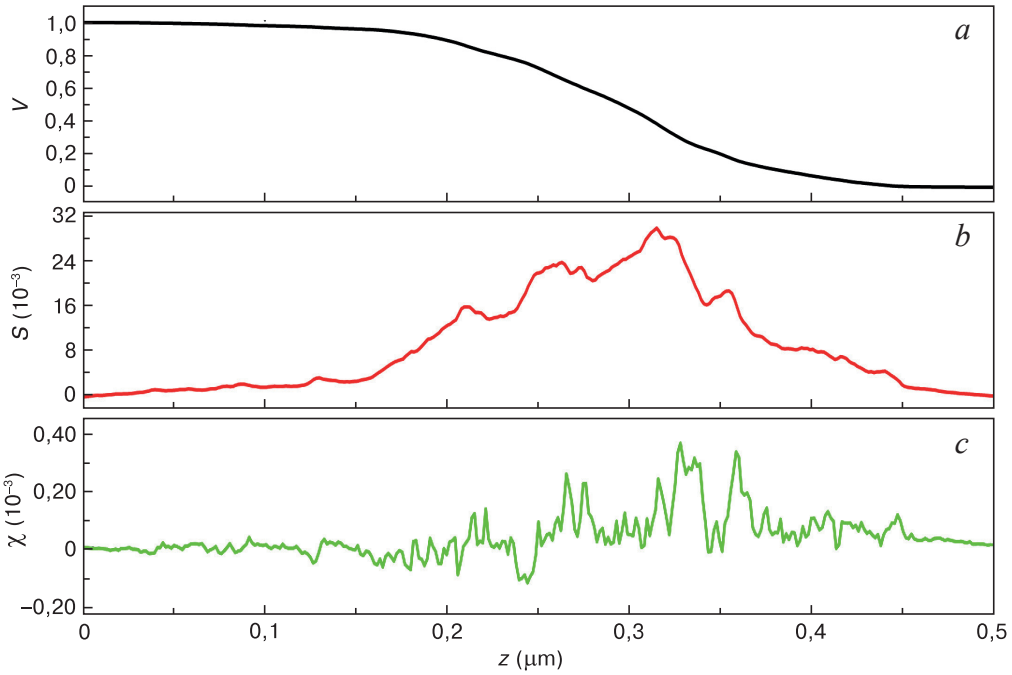

Figure 5. The MFs functionals of the BFOT samples: (*a*) Minkowski volume, (*b*) Minkowski boundary, (*c*) Minkowski connectivity for a scanning area of 5×5 μm^2

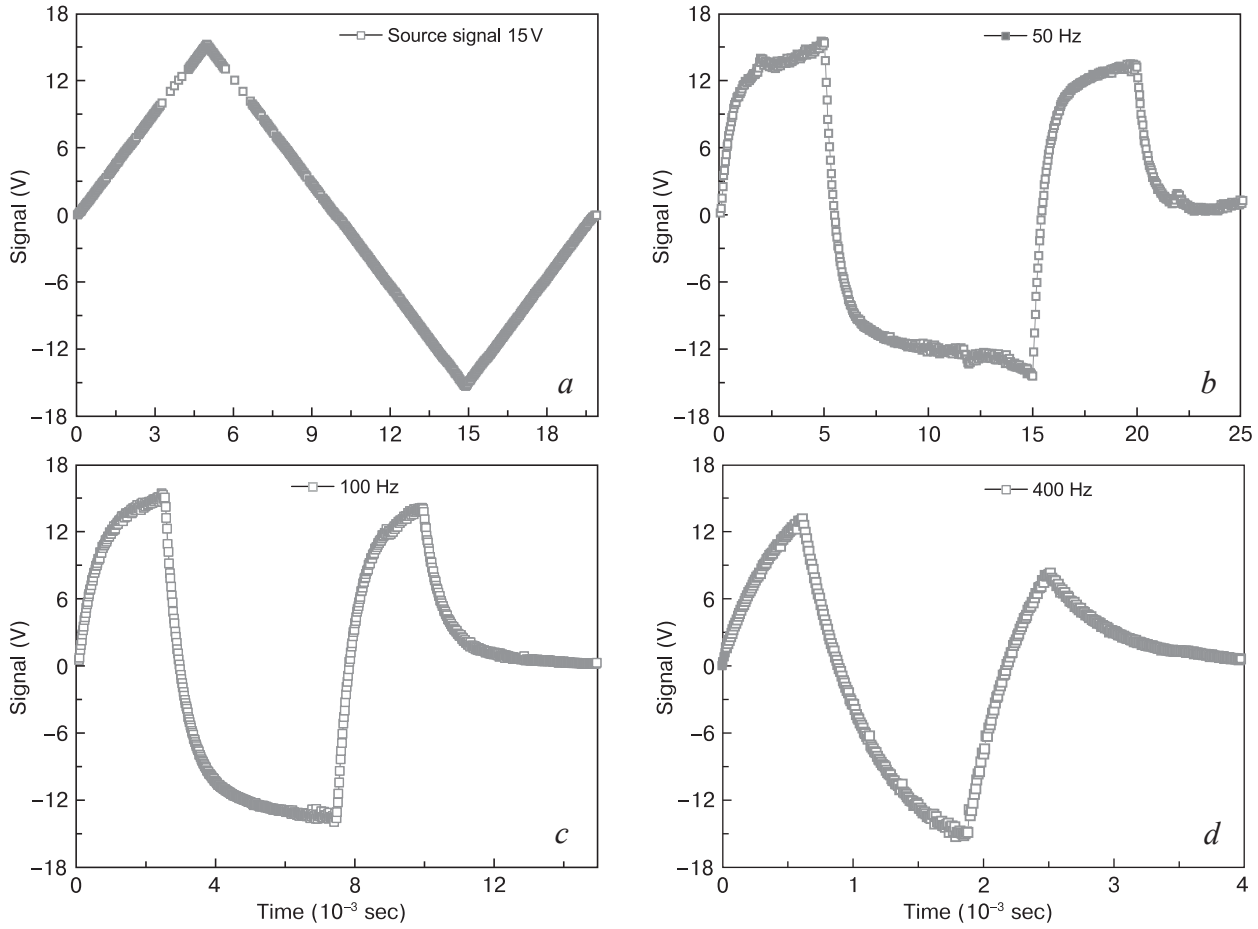

Figure 6. The result of the increase in nonlinearity of the output signal (with a frequency of 50 Hz, 100 Hz, 400 Hz) when applying a bidirectional triangular signal (source signal)

underscores the intricate and irregular nature of the film's topographic patterns.

Hence, the BFOT film exhibits long-range correlations defined by the complex 3D spatial pattern's heterogeneity. Thus, the film's highly rough nature results in intricate and isotropic topographic patterns.

In the BFOT heterostructure, resistance changes occur upon application of voltage, with the formation of phase boundaries and redistribution of oxygen vacancies. Ordered-disordered structural domains arise. Upon application of bias, resistive switching is accompanied by the formation of conductive channels through redox reactions and redistribution of oxygen vacancies [27]. Due to the heterogeneity of the structure, regions of non-uniform conductivity arise in the multicomponent phase. This can result in areas with negative differential resistance (NDR) [28, 29]. The change in current with frequency when applying a bidirectional triangular signal is shown in Fig. 6.

In a high-resistance state, nonlinearity gradually increases due to enhanced polarization and the trapping of mobile charges. In the HRS state, the external field induces an internal volumetric field. Local structural heterogeneities (charge traps) are formed, and depletion of traps leads to a current jump and a sharp increase in the concentration of free carriers [30]. There is a thermal release of trapped electrons into the conduction band, i.e., an internal Schottky effect. Control of the memristor structure was carried out by applying voltage according to $V(t) = M(q(t))I$, where M is the memristance with units of Ω [10].

As seen from Fig. 6, with an increase in frequency, the current increases but the nonlinearity decreases. The hysteresis loop tends to shift towards a straight line and depends on the amplitude, frequency, and duration of the periodic signal. Reducing the signal frequency in dynamic mode promotes an increase in nonlinearity. The resistance of the sample in the high resistance state (HRS) gradually transitioned to the low resistance state (LRS). Frequency measurements in the HRS state showed a transition to the LRS state at frequencies below 50 Hz. With increasing signal frequency, the nonlinearity increases (see Fig. 6).

The SPICE memristor model with negative differential resistance describes this phenomenon through a nonlinear equation of state and a modified window function. When the voltage changes, the memristor model reflects a decrease in current with an increase in the applied voltage, resulting in a negative differential resistance. The window function and threshold voltage help control this behavior, preventing instability. These elements make the model more realistic for applications where memory and nonlinear conduction effects are important [16].

This paper presents the key features for modeling a memristor with nonlinear drift. The state equation describes how the internal state x of the memristor changes under the action of an applied voltage V. The equation takes into account nonlinear effects, describing the dynamic behavior of the memristor over time. The modified Bjoelek window function $W(x)$ allows limiting the change in the memristor state, adjusting it within the permissible values and ensuring the stability of the model. The activation threshold voltage determines the minimum voltage below which the memristor state does not change. This threshold is added to improve the accuracy of the modeling. Figure 7 shows the I–V curve with hysteresis at 0, changed at a signal frequency of 1 Hz. The calculated values are also shown, indicating that the negative resistance increased from 215–440 Ω. This resistance is associated with the dielectric component in this model.

As shown in the Fig. 7, an area of negative differential resistance (NDR) appears [29]. In calculations performed in the LTspice environment, the curvature of this nonlinearity increases with the value of NDR [31]. During the formation of conducting channels in a semiconductor state, the isolating layer of the ferroelectric undergoes a soft breakdown, which causes a sharp current jump with subsequent voltage change. It was found that the current increased while the voltage on the sample decreased, which excluded a hard breakdown in the microstructure of the dielectric. As can be seen in Fig. 6, in the LRS the resistance switches between SET–RESET. The increase and decrease in conductivity within the dielectric layer during the ascending and descending phases of the $I(V)$ curve occurs due to the release of electrons from defect levels described by the Poole–Frenkel conduction mechanism [32, 33]. The phase transformation at the heterostructure boundaries creates conducting and insulating layers.

Thus, as can be seen, the morphological properties, surface roughness, particle size distribution, and topographic patterns, directly influence the pathways for charge carriers, modifying resistive behaviors and affecting mechanisms like NDR and resistive switching. Coatings with high surface roughness exhibit variations in height that lead to uneven electrical fields across the surface. These fields can enhance the polarization within the dielectric

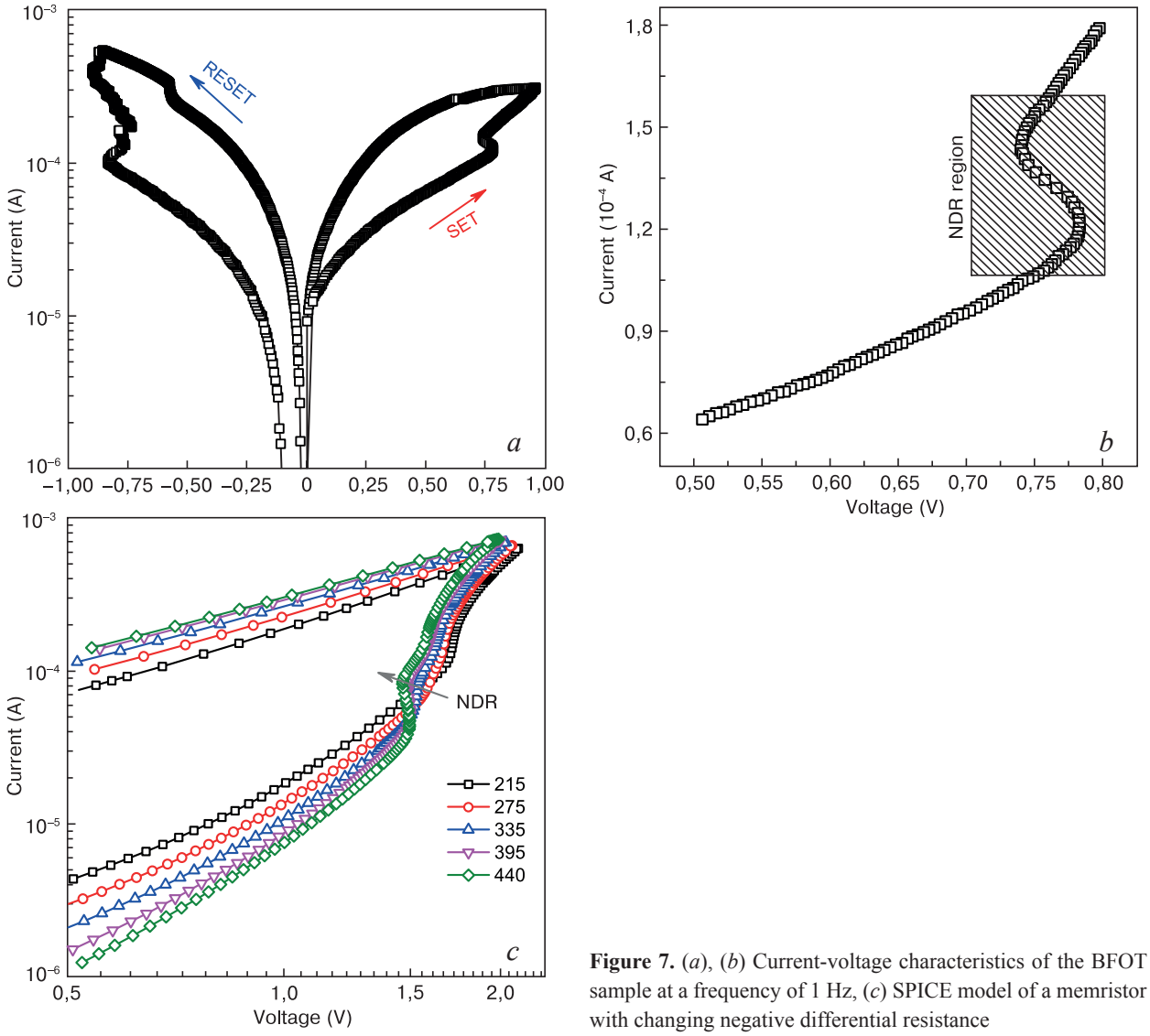

Figure 7. (*a*), (*b*) Current-voltage characteristics of the BFOT sample at a frequency of 1 Hz, (*c*) SPICE model of a memristor with changing negative differential resistance

matrix, leading to charge trapping and the creation of conductive channels. In our BFOT films, the controlled morphology achieved through ALD results in uniform particle distribution, which is critical for consistent electrical performance. The nearly Gaussian distribution of particle sizes suggests a uniform morphology, which aids in achieving stable resistive switching by minimizing localized current pathways that could otherwise lead to dielectric breakdown. The interplay between morphology and electrical properties is further underscored by the presence of topographic features. For instance, the isotropic spatial patterns observed in these coatings enhance the distribution of electric fields, which is advantageous for maintaining consistent switching cycles in memristive applications. Moreover, morphological features such as rough peaks facilitate the formation of self-affine structures that contribute to the exponential decay of autocorrelation functions. This decay indicates the presence of long-range correlations on the film's surface, reinforcing isotropic behaviors that stabilize the electrical response across various frequencies. Thus, the morphology of BFO surface plays a critical role in defining the electrical properties of the coatings, particularly in multiferroic films where surface roughness, grain size, and structural uniformity directly impact charge transport and polarization behavior. Hence, the relationship between morphology and electrical behavior underscores the importance of precise material engineering in developing reliable electronic devices with tailored performance characteristics.

4. Conclusion

Using the ALD method, a BFOT heterostructure was obtained, which exhibits resistive switching properties. After thermal treatment at a temperature of 660 °C during the phase transformation of Anatase/Rutile, the Fe/Ti atom redistribution occurs. Local inhomogeneities and charge trapping centers are formed in the sample. In the HRS state, the conductivity mechanism is mainly associated with spatial bulk charge. In the LRS state, the conductivity mechanism predominantly exhibits tunneling character, possibly related to the Poole–Frenkel. The topographic features were analyzed by morphology methods of the BFOT surfaces, highlighting their spatial patterns, the distribution of heights, self-affine attributes, and the complex and irregular nature of these patterns. Modeling the resistive switching process in the LT spice environment showed a similar region of nonlinearity with an increase in the value of negative differential resistance. Thus, morphological control via deposition techniques like ALD is paramount for tuning electrical properties in BFO coatings. Enhanced understanding of this correlation enables the development of reliable, high-performance devices where electrical properties are dictated by finely controlled topographic characteristics.

Acknowledgments

The work was carried out with the financial support of the Russian Science Foundation grant, project No. 23-22-00421.

Conflict of interest

Authors assuring that, there is no conflict of interest.

References

1. Das R., Sharma S., Mandal K. Aliovalent Ba^{2+} doping: A way to reduce oxygen vacancy in multiferroic $BiFeO_3$. *Journal of Magnetism and Magnetic Materials,* 2016; 401: 129–137. https://doi.org/10.1016/j.jmmm.2015.10.02
2. Fors R., Khartsev S.I., Grishin A.M. Giant resistance switching in metal-insulator-manganite junctions: Evidence for Mott transition. *Physical Review B: Condensed Matter and Materials Physics.* 2005; 71(4): 45305. https://doi.org/10.1103/PhysRevB.71.045305
3. Alikhanov R., Murtazali Kh., Rabadanov M.Kh., Orudzhev F.F., Sultanakhmed Kh., Gadjimagomedov S., Emirov R.M., Sadykov S.A., Kallaev S.N., Ramazanov Sh.M., Abdulvakhidov K., Sobola D. Size-dependent structural parameters, optical, and magnetic properties of facile synthesized pure-phase $BiFeO_3$. *Journal of Materials Science: Materials in Electronics*. 2021; 32: 13323–13335. https://doi.org/10.1007/s10854-021-05911-9
4. Park T.-J., Papaefthymiou G.C., Viescas A.J., Moodenbaugh A.R., Wong S.S. Size-dependent magnetic properties of single-crystalline multiferroic $BiFeO_3$ nanoparticles. *Nano Letters.* 2007; 7(3): 766–772. https://doi.org/10.1021/nl063039w
5. Chua L. Memristor – The missing circuit element. *IEEE Transactions on Circuit Theory*. 1971; 18(5): 507–519. https://doi.org/10.1109/tct.1971.1083337
6. He S., Liu G.-L., Zhu Y.L., Ma X., Sun J., Kang S., Yan Sh., Chen Y., Mei L., Jiao J. Impact of interfacial effects on ferroelectric resistance switching of Au/$BiFeO_3$/Nb:$SrTiO_3$(100) Schottky junctions. *RSC Advances.* 2017; 7(37): 22715–22721. https://doi.org/10.1039/c7ra02339a
7. Xue F., He X., Ma Y., Zheng D., Zhang Ch., Li L., He J.-H., Yu B., Zhang X. Unraveling the origin of ferroelectric resistance switching through the interfacial engineering of layered ferroelectric-metal junctions. *Nature Communications*. 2021; 12(1): 7291. https://doi.org/10.1038/s41467-021-27617-6
8. Schroeder U., Materano M., Mittmann T., Lomenzo P., Thomas M., Toriumi A. Recent progress for obtaining the ferroelectric phase in hafnium oxide based films: impact of oxygen and zirconium. *Japanese Journal of Applied Physics.* 2019; 58(SL): 0801. https://doi.org/10.7567/1347-4065/ab45e3

9. Jiang J., Nguyen L.-A.T., Nguyen T.D., Luong D.H., Kim D.Y., Jin Y., Kim P., Duong D.L., Lee Y.H. Probing giant Zeeman shift in vanadium-doped WSe_2 via resonant magnetotunneling transport. *Physical Review B*. 2021; 103: 014441. https://doi.org/10.1103/PhysRevB.103.014441
10. Deng H., Wang Q. Dynamics and synchronization of memristor-based fractional-order system. *International Journal of Modern Nonlinear Theory and Application*. 2013; 2(4): 223–227. https://doi.org/10.4236/ijmnta.2013.24031
11. Cai Y., Zhang J., Yan M., Jiang Y., Jawad H., Tian B., Wang W., Zhan Y., Qin Y., Xiong S., Cong C., Qiu Z.J., Duan C., Liu R., Hu L. Molecular ferroelectric/semiconductor interfacial memristors for artificial synapses. *npj Flexible Electronics*. 2022; 6: 16. https://doi.org/10.1038/s41528-022-00152-0
12. Orudzhev F., Ramazanov S., Sobola D., Isaev A., Wang C., Magomedova A., Kadiev M., Kaviyarasu K. Atomic layer deposition of mixed-layered Aurivillius phase on TiO_2 nanotubes: synthesis, characterization and photoelectrocatalytic properties. *Nanomaterials*. 2020; 10(11): 2183. https://doi.org/10.3390/nano10112183
13. Orudzhev F.F., Ramazanov S.M., Isaev A.B., Alikhanov N.M.-R., Sobola D., Presniakov M.Y., Kaviyarasu K. Self-organization of layered perovskites on TiO_2 nanotubes surface by atomic layer deposition. *Materials Today: Proceedings*. 2021; 36: 364. https://doi.org/10.1016/j.matpr.2020.04.153
14. Pinelo L.F., Kugel R.W., Ault B.S. Charge-transfer complexes and photochemistry of ozone with ferrocene and n-butylferrocene: A UV-vis matrix-isolation study. *The Journal of Physical Chemistry A*. 2015; 119(41): 10272. https://doi.org/10.1021/acs.jpca.5b07292
15. Nečas D., Klapetek P., Gwyddion: an open-source software for SPM data analysis. *Open Physics*. 2012; 10(1): 181–188. https://doi.org/10.2478/s11534-011-0096-2
16. Mladenov V., Kirilov S. A nonlinear drift memristor model with a modified biolek window function and activation threshold. *Electronics*. 2017; 6(4): 77. https://doi.org/10.3390/electronics6040077
17. Lu C.D., Chang L.S., Lu Y.F., Lu F.H. The growth of interfacial compounds between titanium dioxide and bismuth oxide. *Ceramics International*. 2009; 35(7): 2699–2704. https://doi.org/10.1016/j.ceramint.2009.03.001
18. Ramazanov S., Sobola D., Ţălu Ş., Orudzev F., Arman A., Kaspar P., Dallaev R., Ramazanov G. Multiferroic behavior of the functionalized surface of a flexible substrate by deposition of Bi_2O_3 and Fe_2O_3. *Microscopy Research and Technique*. 2022; 85(4): 1300–1310. https://doi.org/10.1002/jemt.23996
19. Ramazanov S., Orudzhev F., Gajiev G. Surface functionalization of TiO_2 nanotubes modified with a thin film of $BiFeO_3$. *Surfaces*. 2024; 7(1): 1–11. https://doi.org/10.3390/surfaces7010001
20. Xie D., Han X., Li R., Ren T., Liu L., Zhao Y. Characteristics of Pt/$BiFeO_3$/TiO_2/Si capacitors with TiO_2 layer formed by liquid-delivery metal organic chemical vapor deposition. *Applied Physics Letters*. 2010; 97(17): 172901. https://doi.org/10.1063/1.3490712
21. Matos R.S., Pinto E.P., Pires M.A., Ramos G.Q., Ţălu Ş., Lima L.S., da Fonseca Filho H.D. Evaluating the roughness dynamics of kefir biofilms grown on Amazon cupuaçu juice: a monofractal and multifractal approach. *Microscopy*. 2023; 73(1): 55–65. https://doi.org/10.1093/jmicro/dfad040
22. Yu N., Polycarpou A.A. Contact of rough surfaces with asymmetric distribution of asperity heights. *Journal of Tribology*. 2002; 124(2): 367–376. https://doi.org/10.1115/1.1403458
23. Pinto E.P., Matos R.S., Pires M.A., dos Lima L.S., Ţălu Ş., da Fonseca Filho H.D., Ramazanov S., Solaymani S., Larosa C. Nanoscale 3D spatial analysis of zirconia disc surfaces subjected to different laser treatments. *Fractal and Fractional*. 2023; 7(2): 160. https://doi.org/10.3390/fractalfract7020160
24. Ţălu Ş., Nikola P., Sobola D., Achour A., Solaymani S. Micromorphology investigation of gaas solar cells: case study on statistical surface roughness parameters. *Journal of Materials Science: Materials in Electronics*. 2017; 28(20): 15370. https://doi.org/10.1007/s10854-017-7422-4
25. Ramos G.Q., Matos R.S., Das A., Kumar S., Ţălu Ş., da Fonseca Filho H.D. Correlating morphology and multifractal spatial patterns of the leaf surface architecture of anacardium occidentale L. *Fractal and Fractional*. 2022; 6(6): 320. https://doi.org/10.3390/fractalfract6060320
26. Matos R., Ferreira N., Ţălu Ş., Ghaderi A., Solaymani S., Pires M., Sanches E., da Fonseca Filho H. Percolative, multifractal, and symmetry properties of the surface at nanoscale of Cu-Ni bimetallic thin films deposited by RF-PECVD. *Symmetry (Basel)*. 2022; 14(12): 2675. https://doi.org/10.3390/sym14122675
27 Kröger F.A., Vink H.J. Relations between the concentrations of imperfections in crystalline solids. In: F. Seitz, D. Turnbull (Eds). Solid State Physics. Vol. 3. Academic Press; 1956. P. 307–435. https://doi.org/10.1016/S0081-1947(08)60135-6
28. Shen L., Cheng X., Wang Z., Cao D., Zheng L., Wang Q., Zhang D., Li J., Yu Y. Negative differential resistance in the I–V curves of Al_2O_3/AlGaN/GaN MIS structures. *RSC Advances*. 2016; 6(7): 5671–5676. https://doi.org/10.1039/C5RA22356C
29. Felix A.B., Pacheco M., Orellana P., Latgé A. Negative differential resistance in hybrid carbon-based structures. *Physical Review B*. 2019; 99(19): 195442. https://doi.org/10.1103/physrevb.99.195442
30. Ramazanov S., Orudzhev F., Gajiev G., Holcman V., Matos R.S., da Fonseca Filho H.D., Ţălu Ş., Selimov D. Local electrical characteristic of memristor structure in a high-resistance state obtained using electrostatic force microscopy: Fractal and multifractal dynamics of surface. *Applied Surface Science*. 2024; 647: 158863. https://doi.org/10.1016/j.apsusc.2023.158863
31. Chen P., Zhang X., Liu Q., Liu M. NbO_2-based locally active memristors: from physical mechanisms to performance optimization. *Applied Physics A*. 2022; 128(12): 1113. https://doi.org/10.1007/s00339-022-06258-6
32. Schroeder H. Poole–Frenkel-effect as dominating current mechanism in thin oxide films – An illusion?! *Journal of Applied Physics*. 2015; 117(21): 215103. https://doi.org/10.1063/1.4921949
33. Allers K.-H. Prediction of dielectric reliability from I–V characteristics: Poole–Frenkel conduction mechanism leading to $\sqrt{E}$ model for silicon nitride MIM capacitor. *Microelectronics Reliability*. 2004; 44(3): 411–423. https://doi.org/10.1016/j.microrel.2003.12.007